

## SOFT ROBOTS

# Underwater maneuvering of robotic sheets through buoyancy-mediated active flutter

**Junghwan Byun**<sup>1,2,3</sup>, **Minjo Park**<sup>1,2</sup>, **Sang-Min Baek**<sup>1,2</sup>, **Jaeyoung Yoon**<sup>4</sup>, **Woongbae Kim**<sup>1,2</sup>,  
**Byeongmoon Lee**<sup>4</sup>, **Yongtaek Hong**<sup>4</sup>, **Kyu-Jin Cho**<sup>1,2,\*</sup>

Falling leaves flutter from side to side due to passive and intrinsic fluid-body coupling. Exploiting the dynamics of passive fluttering could lead to fresh perspectives for the locomotion and manipulation of thin, planar objects in fluid environments. Here, we show that the time-varying density distribution within a thin, planar body effectively elicits minimal momentum control to reorient the principal flutter axis and propel itself via directional flutter motions. We validated the principle by developing a swimming leaf with a soft skin that can modulate local buoyancy distributions for active flutter dynamics. To show generality and field applicability, we demonstrated underwater maneuvering and manipulation of adhesive and oil-skimming sheets for environmental remediation. These findings could inspire future intelligent underwater robots and manipulation schemes.

Copyright © 2021  
The Authors, some  
rights reserved;  
exclusive licensee  
American Association  
for the Advancement  
of Science. No claim  
to original U.S.  
Government Works

## INTRODUCTION

Thin, planar bodies manifest unique, nonrectilinear paths when they fall or rise freely in a fluid (1). For instance, leaves and paper cards in air, or coins in water, periodically flutter from side to side when falling. Although often seemingly random, extensive theoretical and experimental studies have revealed that this passive flutter dynamics is governed by intrinsic parameters of the moving object and surrounding fluid, such as body geometry, body-to-fluid density ratio ( $\rho/\rho_f$ ), and Reynolds number ( $Re$ ) (2–7). In the well-delineated case of axisymmetric geometry such as a disk (diameter  $D$  and thickness  $t$ ), for example, four distinctive behavioral phases—steady descent, periodic fluttering, tumbling, and chaotic—are explicitly observed and mapped to a “phase diagram” as a function of the dimensionless moment of inertia  $I^*$  ( $=I_{disk}/\rho_f D^5 = \pi t D / 64 \rho_f D$ ) and  $Re$  (fig. S1) (2). Geometries with patterns (8, 9), asymmetric passive appendages (10), linkages (11), and density distributions (12) also yield additional branches of the passive flutter behaviors. Such a series of investigations suggests that even an object lacking in actuation and muscular agility for thrust generation has inherent cues for locomotion in fluids (12–14). In reality, many wingless insects and animals, such as ants (15, 16), frogs (17), and flying lizards (18), demonstrate their aerial maneuverability through instinctive coupling between passive body geometries and air, together with the minimal adjustment of body alignment or rotation for steering control.

Attempts to improve the compactness, flexibility, and adaptability of artificial systems that maneuver through a fluid have been pursued for the last decade (19). In practice, a newer class of robot architectures consisting of soft bodies, muscles, and actuators has clearly demonstrated their strength in mimicking locomotion strategies of biological organisms (20–24) or in achieving intimate interaction with natural environments (25–28), compared with conventional remotely operated vehicles (ROVs), submarines, and other underwater machines. In a similar context, reducing the geometric

form factor of underwater robots to its extreme, e.g., paper sheet-like structure, can maximize the flexibility and adaptability as well as the surface area-to-volume ratio (29–32). Underwater locomotion of such thin, planar system has promise to address some of the existing underwater tasks by much simpler designs that possibly benefit from the capability of folding/unfolding and wrapping. As has been theoretically suggested for decades by several researchers (33–36), the most promising locomotion strategy so far was to achieve undulatory propulsion throughout the whole body. However, exploiting natural flutter dynamics, driven by intrinsic fluid-body coupling, would broaden the perspective of underwater locomotion and manipulation of artificial systems having thin, planar form factors.

Here, we present a strategy for controllable underwater maneuvering of thin, planar bodies, such as a leaf, based on the buoyancy-mediated active modulation of flutter dynamics. We demonstrate how the kinematics and principal axis of flutter behavior can be controlled by means of local buoyancy modulation, and we implemented this governing principle in realizing a “swimming leaf” (movie S1). The swimming ability of thin bodies based on the intrinsic fluid-body coupling, rather than complex muscle patterning and actuation, would provide an unprecedented opportunity for the interaction and transport of many functional systems with extreme form factors.

## RESULTS

### Flutter dynamics modulation by inhomogeneous density distribution

We took initial inspiration from a freely falling leaf with inhomogeneous density distributions (Fig. 1). Recent studies have considered the contribution of internal body torque to symmetry breaking in flutter dynamics (12–14). To investigate this effect in a more general spatial domain, we designed a synthetic leaf with spatially distributed nine mass spots (P0 to P8; Fig. 1, A and B). The point mass integrated onto each spot causes an offset between the centers of mass and buoyancy, which generates an internal body torque coupled with a surrounding fluid (Fig. 1C; see note S2) (12). Although torque modulation is minimally induced by the offset with values smaller than a few percentages of the characteristic length (i.e., wingspan), the resulting effects on the leaf’s flutter dynamics lead to a net propulsive momentum in the offset vector direction (Fig. 1, D to F, and

<sup>1</sup>Soft Robotics Research Center, Seoul National University, Seoul, Republic of Korea.

<sup>2</sup>Biorobotics Lab, Department of Mechanical Engineering, Institute of Advanced Machines and Design, Institute of Engineering Research, Seoul National University, Seoul, Republic of Korea. <sup>3</sup>Physical Intelligence Department, Max Planck Institute for Intelligent Systems, Stuttgart, Germany. <sup>4</sup>Department of Electrical and Computer Engineering, Inter-university Semiconductor Research Center, Seoul National University, Seoul, Republic of Korea.

\*Corresponding author. Email: kjcho@snu.ac.kr

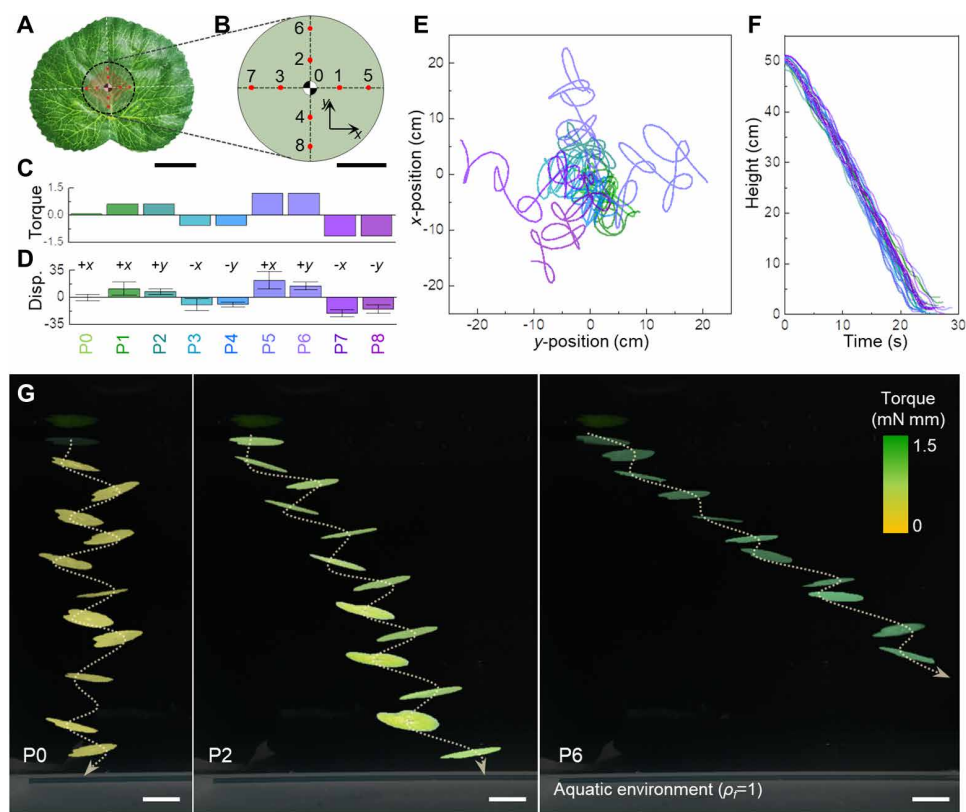


**Fig. 1. Flutter dynamics modulation of a falling leaf by inhomogeneous density distribution.** (A) Schematic of a leaf with inhomogeneous mass distribution defined by nine mass points (P0: initial center of mass; P1 to P8: mass points with 3 mm intervals, numbered in a counterclockwise manner). (B) Magnified schematic of nine mass points. An iron ring with a density of  $7.87 \text{ g cm}^{-3}$  and a weight of 150 mg was used as a point mass. (C) Body torque generated by a point mass located individually in separate mass points defined in (B). (D) Average displacement of the leaf freely falling in water, induced by the torque in (C). The error bars indicate SD. (E) Representative horizontal movements of the falling leaf with a point mass located in different positions (P0 to P8) (see also fig. S2). (F) Time-evolving height difference of the falling leaf shows that body momenta coupled with flutter dynamics modulation dominantly affect net horizontal movement rather than vertical one. (G) Typical falling trajectories suggest that body torque can be a minimal impetus for active modulation of flutter-combined locomotor traits (see also fig. S4). Scale bars, 2 cm in (A), 5 mm in (B), and 5 cm in (G).

fig. S2). This is because the biased downward torque accelerates the rotation of one side and decelerates the other side, creating asymmetrical lifts. Despite the path instability caused by geometric anisotropy, this propulsive momentum regulates the principal axis of flutter behavior, which, in turn, guides the net direction of movement (Fig. 1G and figs. S3 and S4).

### Swimming leaf design based on a buoyancy skin

To show how this flutter dynamics modulation can be used in underwater maneuvering and manipulation of thin, compact systems, we developed a skin-like platform, namely, “buoyancy skin,” that can actively modulate local density (in turn, buoyancy) distributions (Fig. 2, A and B). Out of possible mechanisms for the local density change of elastomers, such as compressed air flow (37) or light-driven crystal phase change (38), the heat-induced liquid-to-gas phase transition was used due to scalability and compactness (39). The buoyancy skin consists of two major components: a liquid-filled elastomer (termed “muscle”) and a soft heating circuit (Fig. 2, A and B, and fig. S5). Analogous to the buoyant cuttlebone function (40) in which

osmotic forces alter the liquid-to-gas ratio to help cuttlefish to efficiently change their density, the muscle here can change its density through continuous and drastic volume changes under an application of heat above the boiling point of the enclosed liquid (Fig. 2C and fig. S5D). In particular, thin, copper (Cu) wires (diameter, 22  $\mu\text{m}$ ) were connected to deliver sufficient power to the heating circuit without effective structural interference. Geometries of the muscle and electronic circuitry take the form of an axisymmetric, regular hexagonal structure with spatially distinct three activation sites for efficient spatiotemporal body torque modulation (Fig. 2, D and E). Provided that the mass distribution is uniform throughout the muscle, the active heat modulation could continuously change the volume and the corresponding density and buoyancy distributions. The result, in turn, leads to the occurrence of the triangular domain of the offset vector ( $\delta$ ) between the centers of buoyancy and gravity (Fig. 2E, bottom).

The buoyancy generation ( $\Delta F_B$ ) and the corresponding density changes induced by the buoyancy skin are characterized by the profiles in Fig. 2F. Given the nature of phase transition,  $\Delta F_B$  curves could not be a step function. Instead, we found that this buoyancy profile arises from unique underwater heat responses generated by the heating circuit (fig. S6, A and B). As a result, the characteristics of the temporal buoyancy response could be normalized regardless of the heating condition and actual saturation value, and we could estimate them by two-part

exponential decay curves (Fig. 2G and figs. S6C and S7; see Materials and Methods). Specifically,  $\Delta F_B$  reaches (or loses) 80% of the saturation value within  $\sim 22$  s under heating (or  $\sim 18$  s under cooling). The resultant  $\Delta F_B$  capacity was reliable and repeatable (Fig. 2H), and its operation window (accessible  $\Delta F_B$  range) could be engineered to be  $\sim 5.6$  mN depending on the input current level (Fig. 2F) and muscle thickness (fig. S6D). We observed that the design and  $\Delta F_B$  capacity of our buoyancy skin were optimized to reverse the sign of the net buoyancy-corrected gravity of the leaf, allowing it to take off and stabilize to flutter through the path analogous to that of a falling leaf (Fig. 2I, fig. S8, and movie S1). This active lifelike behavior was an experimental demonstration where a single geometry experienced flutter paths continuously throughout the falling and rising motions.

### Analysis on buoyancy skin-mediated active flutter

Active buoyancy control through the buoyancy skin fundamentally fuels flutter dynamics and its modulation in two ways: (i) Uniform  $\Delta F_B$  changes the overall density and the corresponding kinematic parameters such as velocity (or  $Re$ ) and frequency, and (ii) spatial

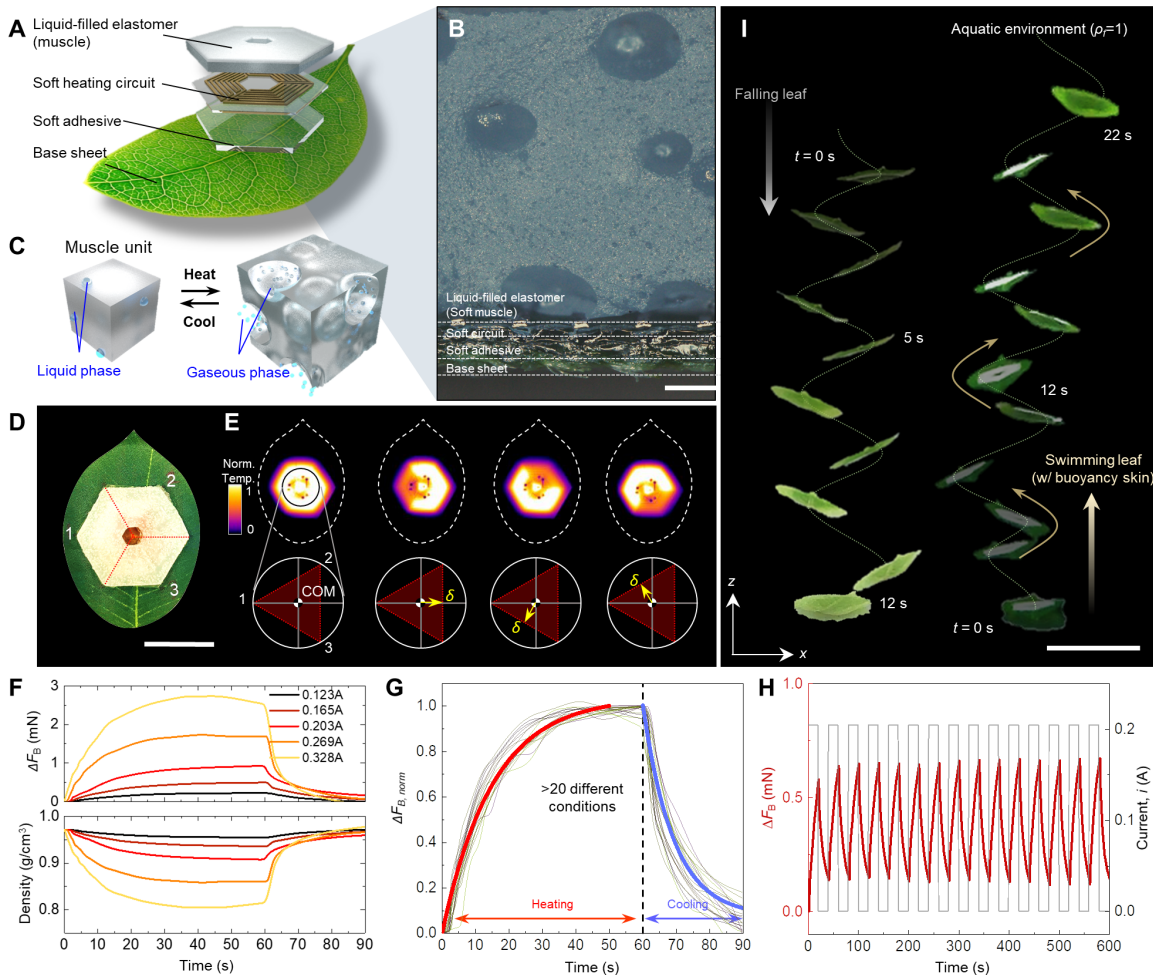


**Fig. 2. A swimming leaf based on a buoyancy skin.** (A) Exploded-view schematic illustration of a swimming leaf consisting of a buoyancy skin and a base sheet (leaf). (B) Optical cross-sectional image of a swimming leaf. (C) Operating mechanism of a buoyancy-control muscle. When heated, the liquid enclosed by the elastomer transits from the liquid to gaseous phase, producing continuous and drastic volume changes of the muscle. (D) Photograph of a leaf integrated with a buoyancy skin. (E) Thermographic images (top) and the corresponding offset vectors,  $\delta$ , (bottom) in response to uniform and nonuniform buoyancy distributions. (F) Buoyancy generation ( $\Delta F_B$ ) profiles and the corresponding density changes of a 2-mm-thick muscle in response to varying input currents. (G) Normalized buoyancy profiles obtained under more than 20 different operating conditions about current levels, muscle thicknesses, and activation areas. (H) Cyclic buoyancy profile in response to a  $0.025\text{-s}^{-1}$  square wave input current of amplitude 0.204 A. (I) Composite images of a falling and swimming leaf. The uniform  $\Delta F_B$  generated by electric current of 0.282 A allows the leaf to swim through a fluttery path. Thin, insulated Cu tethers were connected to transfer power. Scale bars, 500  $\mu\text{m}$  in (B), 2 cm in (D), and 5 cm in (I).

$\Delta F_B$  distribution produces body torques that reorient the principal flutter axis, providing a dynamic cue for versatile fluttery swimming gaits (Fig. 2E). To investigate these effects, we first minimized the geometric anisotropy by proposing a circular disk-shaped base sheet (diameter  $D$ ). We established an empirical geometric criterion in which the flutter dynamics of a buoyancy skin-integrated disk, considered simply as a stacked disk, can be approximated by that of a homogeneous disk with density  $\rho$  and effective thickness  $t^*$ , which reads as

$$\left(\frac{\rho}{\rho_f} - 1\right) \left(\frac{t^* - t_1}{D}\right) < 0.001$$

where  $t^* \approx p_1 t_1 / \rho + (p_2 t_2 / \rho)(a/D)^4$ ,  $(\rho_1, D, t_1)$ , and  $(\rho_2, a, t_2)$  are the density, diameter, and thickness of the base disk and muscle, respectively (fig. S9; see note S1 for details). On the basis of this criterion, we

defined the swimming disk design that satisfies  $(\rho/\rho_f - 1)(t^* - t_1)/D = 2.23 \times 10^{-4}$  and  $I^* \sim 7 \times 10^{-4}$  (Fig. 3B, inset). In this design, uniform muscle activation changes the overall density from  $1.02$  to  $0.86 \text{ g cm}^{-3}$  in response to tunable input currents ranging from  $0$  to  $0.35$  A (Fig. 3, A and B). This tunable density enabled a single, predefined disk to actively change the flutter behaviors, realizing a “swimming disk”: The disk was initially stationary in an aquatic environment ( $\rho_f = 1 \text{ g cm}^{-3}$ ), began to take off with  $\Delta F_B \approx 0.25 \text{ mN}$ , and exhibited periodic upward fluttering motions characterized by frequency  $f = 0.1$  to  $0.35 \text{ s}^{-1}$ , amplitude  $A = 1.1$  to  $2.5 \text{ cm}$ , and vertical velocity  $U_z = 0.98$  to  $2.56 \text{ cm s}^{-1}$  under  $\Delta F_B = 0.26$  to  $1.68 \text{ mN}$  (Fig. 3, C and D, fig. S10, and movie S2). These results show good agreement with theoretical values particularly for  $Re$ , which is expressed by  $[2t^*g(1 - \rho/\rho_f)]^{1/2}D/v$  based on the terminal velocity with a square drag term in modest  $\Delta F_B$  ranges above which wake instability disturbs flutter kinematics (Fig. 3C). It is also identified that the resultant

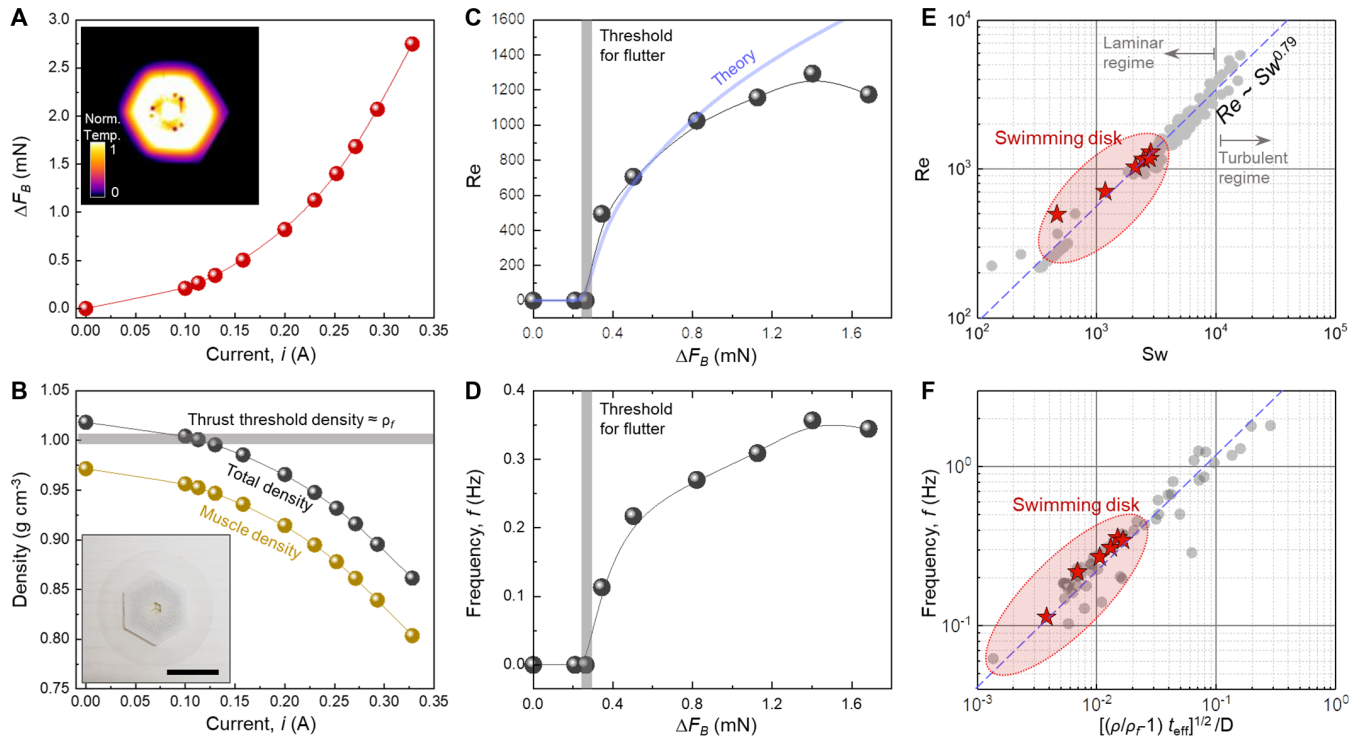


**Fig. 3. Active flutter dynamics under uniform buoyancy distributions.** (A) Active modulation of the saturated  $\Delta F_B$  of a typical 2-mm-thick muscle in response to uniform heating with varying input currents. The inset shows a typical thermographic image of uniform heating. (B) Active modulation of muscle density (yellow) and the corresponding changes in the total density of a standard swimming disk (gray) under  $\Delta F_B$  in (A). The inset image shows the design of a standard swimming disk. Scale bar, 2 cm. (C and D) Buoyancy-mediated active modulation of the flutter behavior of a swimming disk that has geometric form factors of ( $\rho_1, D, t_1, \rho_2, a$ , and  $t_2$ ) = (1.334 g cm<sup>-3</sup>, 45 mm, 0.125 mm, 0.971 g cm<sup>-3</sup>, 32 mm, and 2.085 mm) satisfying  $(\rho/\rho_f - 1)\Delta t^*/D = 2.22 \times 10^{-4}$  (movie S2). (E and F) Characterization of the buoyancy-mediated active flutter of the swimming disk (red) in comparison with the passive flutter of falling disks (gray) in frequency (E) and  $Re$ - $Sw$  (F) domains (41).

dynamics and maneuvering window hew to the deterministic scaling relation of falling disks in terms of  $f$  (Fig. 3E) and dimensionless swimming number [ $Sw = 2\pi fAD/v$ , where  $v$  is the kinematic viscosity (41)] (Fig. 3E and fig. S11), both of which validate the effectiveness of our design criterion.

Spatially nonuniform  $\Delta F_B$  distribution induces the specific offset vector ( $\delta$ ) between the centers of buoyancy and gravity, which has symmetry in dynamics with those originated from mass distributions as depicted in Fig. 1 (Fig. 2E and fig. S12). Typical control commands, in which two of the three sites are coupled, are used to generate  $\delta$  at 120° intervals, and their combinations form the accessible triangular  $\delta$ -space (red area) within which the movement of the center of buoyancy is limited (Fig. 2E). The biased  $\delta$ , together with time-varying  $\Delta F_B$ , produces an internal body torque ( $\tau = |\delta|\Delta F_B \cos\theta$ ), which has the maximum experimental value of ~5.2 mN/mm in our design (fig. S13). Simultaneously coupled with the surrounding fluid dynamics,  $\tau$  modulates the upward flutter dynamics by generating net propulsive momentum as discussed in Fig. 1 (Fig. 4, A and B, and movie S3). The analysis on the resulting behaviors qualitatively verifies that  $\delta$  modulation reorients the flutter axis with some delays and accordingly determines the average direction of motion (Fig. 4B, right inset, and fig. S14). In addition, we see that the contribution of  $\tau$  to flutter dynamics modulation yields inverse and linear correlations with the path angle ( $\psi$ ) and horizontal velocity ( $U_x$ ), respectively (Fig. 4, C and D), which are in good agreement with predictions from numerical and experimental studies of falling objects (12, 13).

The maximum performance of the swimming disk with  $D = 45$  mm achieved  $U_x$  of ~2 cm s<sup>-1</sup> (=0.44 body length/s) with  $\psi$  of ~35°.

### Time-evolving flutter axis reorientation for fluttery swimming gaits

Temporal variations in  $\Delta F_B$  distribution (or  $\delta$ ) induce a sequential reorientation of the principal flutter axis, showing the potential of various fluttery swimming gaits. To investigate such behavior, we compared the flutter behaviors of the swimming disk responding to three representative  $\delta$  instructions driven by uniform, nonuniform, and clockwise time-varying nonuniform  $\Delta F_B$  distributions (Fig. 5A). As shown in Figs. 1G and 4, the flutter axis is randomly oriented for uniform  $\Delta F_B$  distribution (i.e.,  $\delta = 0$ ), whereas  $\delta$  originated from nonuniform  $\Delta F_B$  distribution triggers directional symmetry breaking in overall flutter dynamics, achieving horizontal drifts characterized by the alignment of the flutter axis with  $\delta$  (Fig. 5, B and C, top and middle, and fig. S14). Our key observation here is that additional changes of  $\delta$ , easily instructed by temporal combinations of the commands shown in Fig. 2E, sequentially drive flutter axis reorientation in ways that follow and, more ideally, reach the direction of  $\delta$  (Fig. 5, B and C, bottom; fig. S15; and movie S4). This attractive movement was the outcome of the time-varying active flutter, and it could be controlled in a desired manner by modulating  $\delta$  profiles in time domain (fig. S15). Representative  $U_x$ - $U_y$  relationships further support the flutter axis reorientation and the corresponding style of movement (fig. S15, E to G).

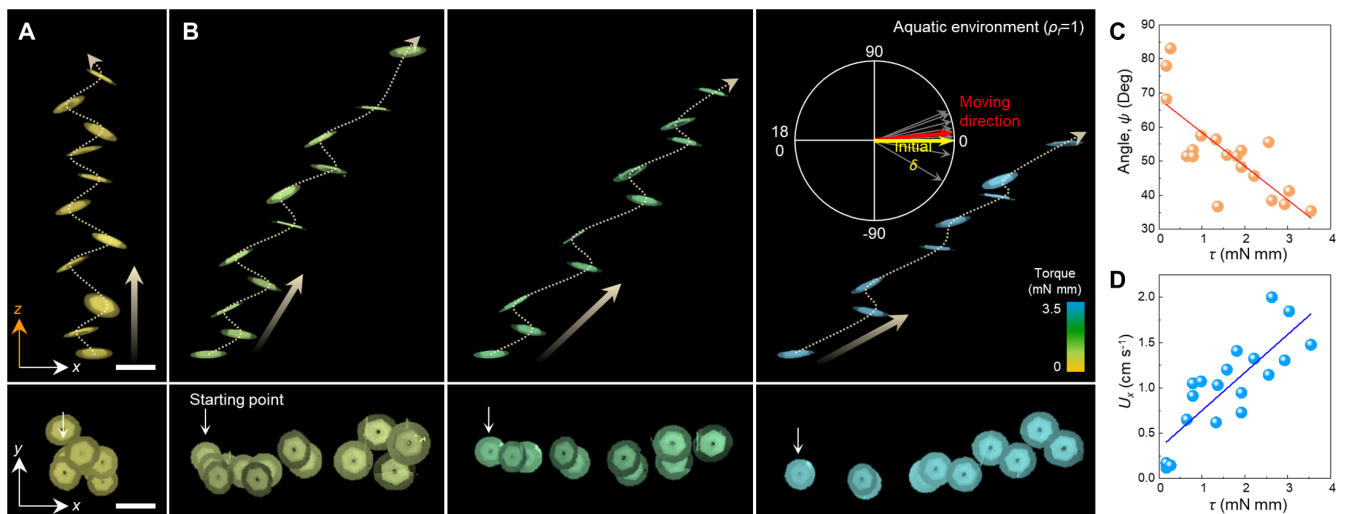


**Fig. 4. Directional active flutter under nonuniform buoyancy distributions.** (A and B) Body torques generated by  $\delta$  in Fig. 2E modulate overall flutter dynamics in ways that not only align the principal flutter axis but also produce directional propulsion (see also figs. S13 and S14 and movie S3). Scale bars, 5 cm. (C and D) Path angle,  $\psi$  (C), and horizontal speed,  $U_x$  (D), of the directional fluttery gaits as a function of  $\tau$ .

Achieving directional propulsion and steering control by buoyancy-mediated minimal body torques offers a new strategy for underwater maneuvering and manipulation of thin, flat bodies. To highlight the effectiveness of this principle, we demonstrated that the leaf could swim in a 90 cm-by-90 cm-by-60 cm space (Fig. 5, D and E, and movie S5). We first developed a set of gait protocols based on time-varying combinations of seven different control commands (fig. S16). This simple protocol allowed us to accomplish desired forward/backward and left/right turning gaits with depth maintenance that is necessary to prevent the leaf from reaching the surface of water (fig. S17). Although the geometric anisotropy of the leaf complicated the quantitative interpretation of the flutter dynamics, the overall motions of the leaf could be controlled and maneuvered solely by buoyancy-mediated active flutter (Fig. 5, D and E). Upon sequential command combinations, we see that  $\delta$  time-dependently moved on the leaf. Such effects effectively modulated flutter dynamics to demonstrate consecutive rising and falling motions that combined multiple forward and turning gaits with the fluttery nature (fig. S18). The resulting journeys were characterized by the trajectories of a “star” (Fig. 5D) and “3” (Fig. 5E) with an average speed of  $\sim 1.5 \text{ cm s}^{-1}$  over a total distance of  $\sim 400 \text{ cm}$ , which is 85 times longer than the leaf’s body length (fig. S18D and movie S5).

### Multifunctional swimming robotic sheets

The principle of buoyancy-mediated active flutter can be a generic locomotor trait of functional platforms formulated in thin, planar geometry. The unique merits of the sheet-like robot design and the fluttery swimming strategy include compactness, flexibility, adaptability, and several related functions originated in the large surface area-to-volume ratio. To show potential applications, we present some proof-of-principle scenarios of multifunctional swimming robotic sheets that can negotiate undesirable environments and/or perform environmental remediation in terms of underwater plastic debris (42) and oil spills (43). First, we fabricated a highly flexible swimming sheet and challenged it to pass through a gap whose size (4 cm) is less than half of the robot (10 cm) (Fig. 6A, fig. S19, and movie S6). We modified the standard design of the swimming disk,

as shown in Fig. 3B, by replacing a 4.5-cm and 125- $\mu\text{m}$ -thick polyethylene naphthalate (PEN) (Young’s modulus,  $\sim 5 \text{ GPa}$ ) base sheet with a 10-cm and 25- $\mu\text{m}$ -thick thermoplastic polyurethane (TPU) (Young’s modulus,  $\sim 14 \text{ MPa}$ ) base sheet (fig. S19A); the bending stiffness was reduced by five orders of magnitude. Sequential control protocols of directional and vertical active fluttery gaits allowed the robot to reach, negotiate, and pass through the gap by structural adaptation of the whole body. Next, we incorporated a wet-tolerant adhesive sheet with an adequate buoyancy skin to investigate the intimate interaction with and removal of underwater plastic debris (Fig. 6B). The geometry of the swimming robotic sheet featured a web-like kirigami structure that increases conformability and thus the probability of physical interaction (fig. S20A). The used buoyancy skin has a muscle configuration that is more spatially distributed to easily adjust the body torque. The sequential control protocol allowed the sticky robotic sheet to approach and perform environmental remediation by carrying plastic debris toward the surface of water (Fig. 6B and movie S7). The last scenario demonstrates large-area oil-skimming capabilities by combining origami design (Fig. 6C). In this case, the swimming robotic sheet integrated a bioinspired self-deploying origami frame (44), superhydrophobic-superoleophilic sorbent sheets (HP-156, 3M; 16 units, each 18 mm by 18 mm), and an adequate buoyancy skin (fig. S20D). The total oil absorbency of the robotic sheet was  $\sim 16.3 \text{ g}$  [ $>1200$  weight % (wt %) of the sorbent sheet units] (fig. S20, H and I), and the embedded origami structure permitted both rapid unfolding ( $<6.4 \text{ s}$  in water) and self-locking, which supported reliable swimming under hydrodynamic drags (Fig. 6D). A series of motions including placement, origami deployment, skin activation, controlled maneuvering, and oil skimming showcases an attractive solution to the long-standing marine environmental and engineering problems, by fully exploiting the thin geometric nature of the swimming robotic sheets (Fig. 6E and movie S8).

### DISCUSSION

Inspired by how the falling trajectory of a leaf could be changed by inhomogeneous density distributions, we have shown that the

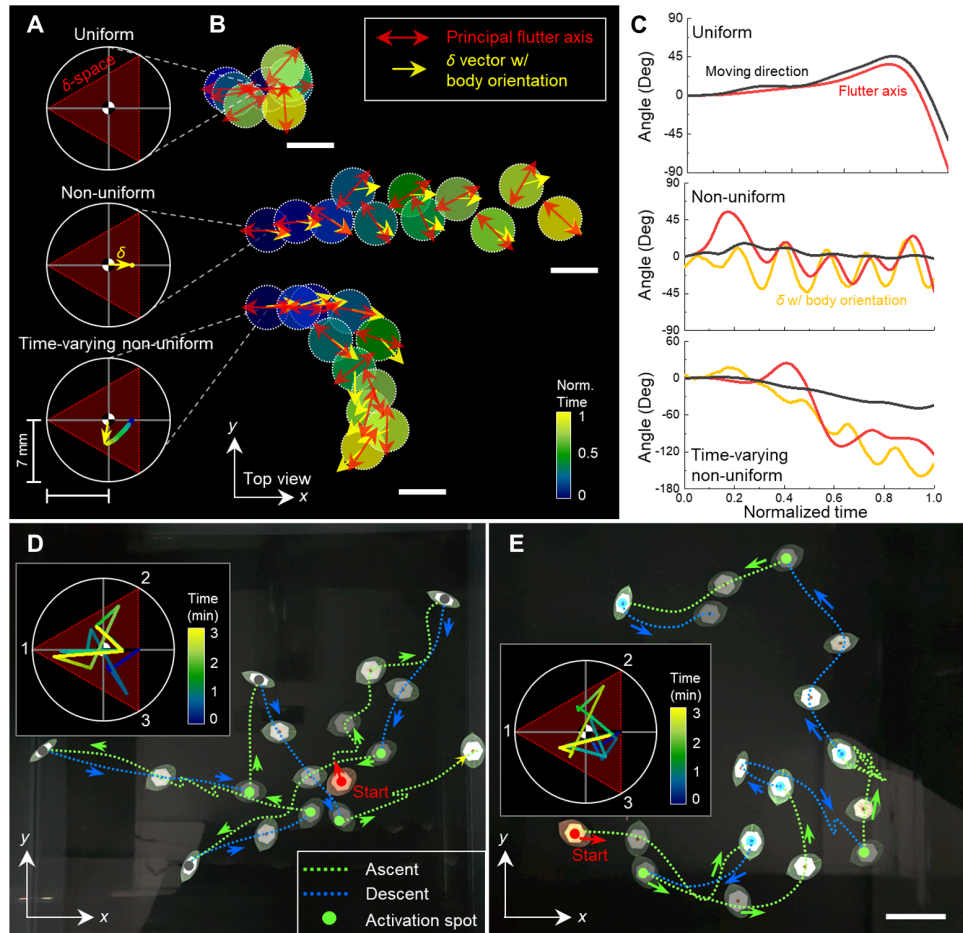


**Fig. 5. Fluttery swimming gaits through sequential reorientation of the principal flutter axis.** (A) Typical profiles of  $\delta$  vectors responding to uniform, nonuniform, and time-varying nonuniform buoyancy distributions. (B) Fluttery swimming gaits of a disk driven by buoyancy-mediated active flutter with  $\delta$  instructions in (A), represented by the normalized time. (C) Time-evolving reorientation of  $\delta$  (adjusted with the body orientation, yellow), flutter axis (red), and overall body movements (black) of a swimming disk in (B). (D and E) Two scenarios of long-term journeys of a swimming leaf (design is shown in Fig. 2E) steered by sequential combinations of control commands defined in fig. S16C (movie S5). Inset images show time-varying  $\delta$  vectors. All swimming experiments were powered externally by thin, insulated Cu wires. Scale bars, 5 cm in (B), and 10 cm in (E).

flurry gaits, originating in the generic nature of fluid-coupled thin bodies, can be controlled through local buoyancy modulation and leveraged for unique locomotion modes of bodies lacking in muscular components. Such a principle was accomplished solely by a soft, thin, compact skin, without any conventional propellers, servomotors, pneumatic or hydraulic artificial muscles, or short-range phototactic and magnetic steering. The outcome was unique functionalities originating in thin and flexible form factors that were previously unattainable by conventional ROVs, submarines, underwater gliders, and other emerging underwater soft robots; for example, the buoyancy skin-integrated swimming robotic sheets could be folded/unfolded for large-area field applications (Fig. 6) and wrapped around various surfaces for better interaction with surrounding environments (fig. S21 and movie S9), as in the case of electronic (45) and robotic (46) skins that activate inanimate objects. Similarly, the capabilities to modulate local density distribution on the body lacking in actuation and muscular agility (fig. S21) have the potential to

directly transport various onboard electronics (e.g., printed circuit boards, sensors, display, and solar panels) and membrane/patch-type function (e.g., oil-water separation, drug delivery, and chemical adsorption) without any underwater carrier machine.

With respect to locomotion strategy and performance, the buoyancy-mediated active flutter principle can be a generic locomotor trait of thin, planar bodies at scales ranging from a few millimeters to meters over which flutter dynamics governs the motion ( $Re > 100$ ; see fig. S1). This principle is not only effective in vertical movement-combined motions but also complementary to the existing directional propulsion mechanisms, such as helical propulsion (20) and undulatory swimming (47). The total energy conversion efficiency ( $\eta_{\text{total}}$ ) is  $\sim 1.88 \times 10^{-4}$  (%), which is comparable with other mobile soft robots (48) due to the inefficiency of Joule heating (see note S4). However, the efficiency could be improved by using a low-melting-point liquid or an optimized muscle and heater design.

The naturally occurring turbulence is also an essential factor to consider for realistic locomotion. Our experimental results show that the turbulence flow negatively influenced on the gait of the swimming sheets; in particular, the vertical flow was disadvantageous to our robot design (fig. S22). Precise steering of fluttery gaits was still difficult when the turbulence effect was much larger than the size and power of the swimming sheet despite efforts to control the robot during turbulent flow. Conversely, however, we can envision that the sheet-like design, which is easily affected by current flows due to its lightweight and large surface area properties, could travel long distances in a very energy-efficient way, if followed by further optimizations.

The untethered version of the proposed locomotion strategy is also an important ingredient for better applicability to aforementioned real-world tasks. Although the demonstrations of the swimming robotic sheet prototypes that performed underwater missions in unprecedented ways, as shown in Fig. 6, successfully verified the feasibility of practical functions, it is ultimately necessary to bridge the gap between the tethered and untethered robot design. Possible approaches to wirelessly transmit power for local buoyancy modulation include magnetothermal effects (49) and laser-driven heating (38). However, the constraints of workspace, system appendages, and line of sight are outstanding challenges. The integration of thin-film batteries is another promising candidate (50), but structural and/or performance optimization and encapsulation should be addressed. Although power transmission and efficiency issues should

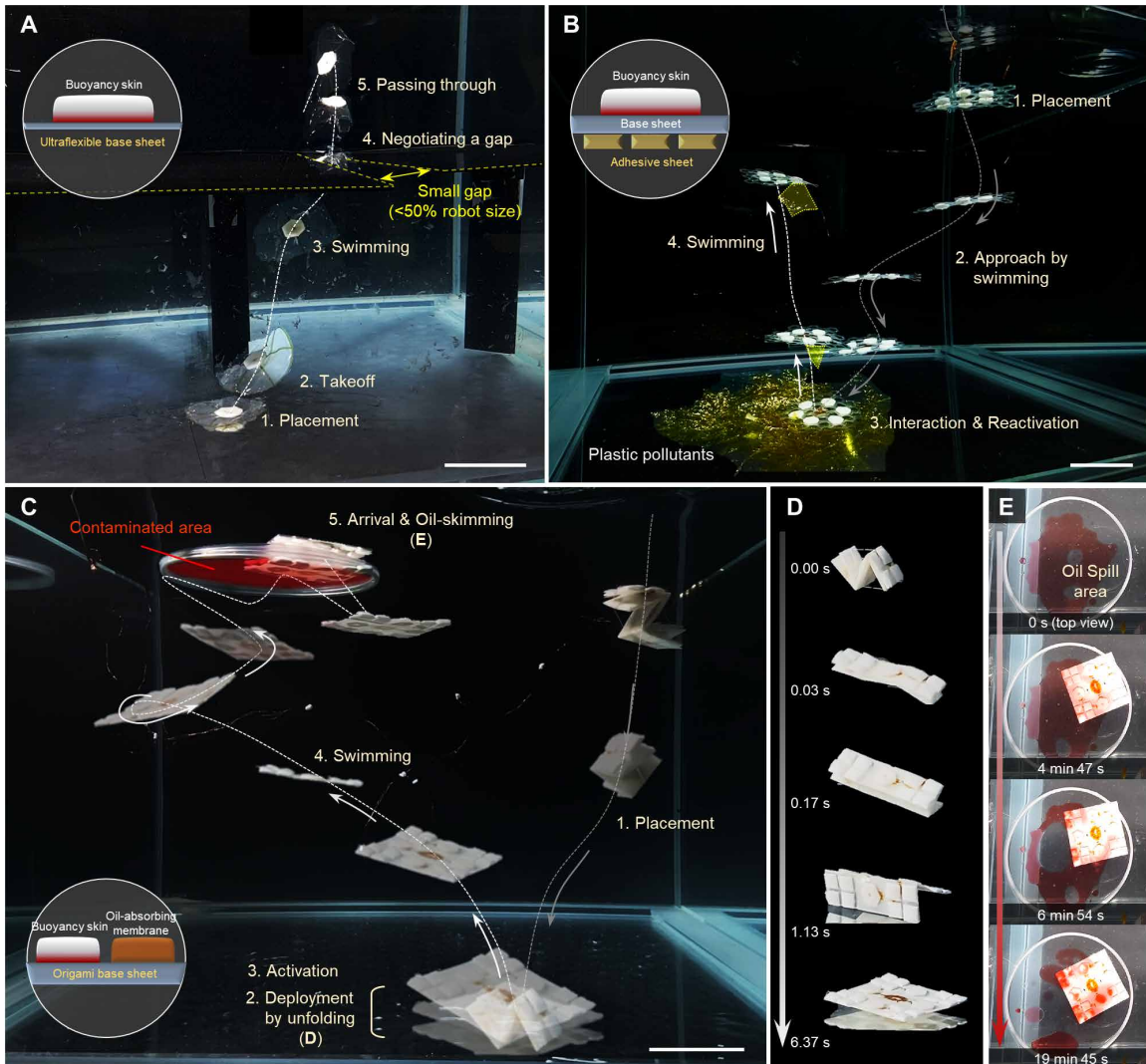


**Fig. 6. Demonstration of multifunctional swimming robotic sheets driven by buoyancy-mediated active flutter.** (A) Composite images of a swimming ultrathin robotic sheet that negotiates a small gap (movie S6). (B) Composite images of a swimming robotic adhesive sheet for the removal of marine plastic pollutants (movie S7). (C) Composite images of a swimming robotic oil-skimming sheet for the removal of oil spills (movie S8). The contaminated area (highlighted in red) is bounded by a circular tube with a diameter of 30 cm. (D) The robotic origami sheet can be deployed within a few seconds and self-locked using a ladybird beetle–inspired compliant origami mechanism (44). (E) Image sequence of the successful oil-skimming through underwater maneuvering. All experiments were performed inside the water chamber with dimensions of 90 cm by 90 cm by 60 cm and powered externally by thin, insulated Cu wires. Scale bars, 10 cm.

continue to be discussed, we expect that time-varying density distribution in thin, flexible systems and their flutter-combined underwater locomotion strategy could be a step toward a new generation of intelligent, naturally adaptive underwater robots.

## MATERIALS AND METHODS

### Falling leaves with inhomogeneous mass distribution

A synthetic leaf design was selected and reproduced by laser cutting a 125- $\mu\text{m}$ -thick PEN (Teonex Q51, Plastic Films Company Ltd.) film (density, 1.347 g  $\text{cm}^{-3}$ ). Nine mass points were defined with 3-mm intervals (Fig. 1B), and a point mass (iron ring, density of 7.87 g  $\text{cm}^{-3}$  and weight of 150 mg) was assembled onto each spot by a double-sided adhesive tape. The addition of the point mass shifts the center of mass position by 0.46875 mm for P1 to P4 and 0.9375 mm for P5

to P8, respectively. For each mass distribution, 12 to 18 free-fall experiments were conducted inside the water chamber with dimensions of 90 cm by 90 cm by 60 cm. We observed that flutter behaviors, directionally guided by an internal body torque, were composed of three typical types of flutter cycles, each of which consists of a pair of forward and backward flutter edges (fig. S3, A and B). Therefore, a principal flutter axis could be defined within a horizontal domain, and its time-evolving reorientation was investigated in comparison with  $\delta$  (fig. S4).

### Fabrication of a swimming leaf and disk

The soft heating circuit was made using a conventional fabrication method of flexible printed circuit boards. A heat-tolerant 12- $\mu\text{m}$ -thick PEN film was bonded with a stainless steel roll sheet (25  $\mu\text{m}$ ; SUS304) using epoxy resin (25  $\mu\text{m}$ ; HGB-E250WG) and then pressed at

150°C for 30 min. Subsequent photolithography and wet etching in hydrochloric acid were performed to obtain well-defined heating circuits (width of 100 μm and pitch of 400 μm). The soft heater's performance depends on several factors such as geometry, electrical resistance, and operating environment (air or water). Here, we used a regular hexagon-shaped circuit (fig. S5) divided into three separate regions with serpentine wiring components to match the resistance with sufficient levels. For the hexagonal heater with sides of 12 mm, the initial resistance was ~230 ± 10 ohms, and it could be stably maintained under cyclic bending and folding. The mass-produced heating circuits were then attached to heat-tolerant, soft, double-sided adhesives (thickness, 175 μm; 300LSE, 3M) and cut into a 16-mm-side hexagon by a CO<sub>2</sub> laser cutter (VLS3.50, Universal Laser Systems). Thin, insulated Cu tethers (diameter, 22 μm; Tianjin Ruiyuan Electric Material Co. Ltd.) were then connected to the prepared circuits via silver epoxy (ABLESTIK 84-1LMISR4, Henkel), and the circuits were passivated by Kapton (12.5 μm) to prevent the robot from direct water contact.

The liquid-filled elastomer muscle is made of Ecoflex 0050 (Smooth-On Inc.) and ethanol (99.9%; Daejung Chemicals & Metals Co. Ltd.). Using a previously reported fabrication method (29), we dissolved 16.7 wt % ethanol in the part A and B mixture of Ecoflex 0050 and stirred for about 5 min. The mixture was then poured onto three-dimensional (3D) printed polylactic acid molds (constructed using Ultimaker 3) and cured for 2 hours at room temperature (~22°C). The muscle takes the form of a thin regular hexagonal column (fig. S5D), whose sides are 16 mm, which is defined to be 4 mm longer than that of the heating circuit to fully transfer the generated heat energy to the muscle. In particular, the center hole (hexagonal column with sides of 3 mm) was formed into the hexagonal geometry not only to provide a space for electrical tethers (Cu, diameter, 22 μm; Tianjin Ruiyuan Electric Material Co. Ltd.) but also to improve the cooling efficiency by increasing the contact area with water. Thickness is easily tunable from 1 to 5 mm depending on the effective  $t^*$  range and target demonstration, and this variation results in the control of buoyancy density from 0.35 to 2 mN cm<sup>-2</sup> (fig. S6D). For the ease of characterization for several demonstrations, we fixed the geometry and dimension of the unit muscle as a 16-mm-side regular hexagon with a thickness of 2 mm and then normally increased the number of muscles and changed their configurations to meet target applications.

There is a wide space for the choice of materials for a base sheet. Given the heat-driven mechanism and ease of initial density engineering, heat-tolerant polymeric materials are preferred. Among several candidates, we mainly used PEN sheets, which offer thermal stability up to 200°C. We cut a PEN sheet with a thickness of 125 μm into the circular or leaf geometry and completed the assembly with the muscle part for demonstrations of the swimming disks and leaves.

### Design and fabrication of swimming robotic sheets

The underwater maneuvering principle via buoyancy-mediated active flutter is a priori material independent, and its operation window can be easily engineered to endow swimming capabilities on a variety of objects, similar to electronic (45) and robotic (46) skins that can activate inanimate objects (fig. S21). To show potential applications (42, 43), we developed three types of underwater machines with design as thin as a paper sheet, namely, “swimming robotic sheets”: the first one is for the negotiation of a small gap (fig. S19) and the other two for the removal of underwater plastic debris (fig. S20, A to C)

and oil spills (fig. S20, D to I). The robotic sheet for the gap negotiation was designed by modifying the standard swimming disk. To showcase its extreme flexibility, we used a thinner (thickness, 25 μm) and softer TPU material (Young's modulus, 14 MPa) as a base sheet. In particular, we added thin Kapton frames (thickness, 12.5 μm) to compensate the swimming reliability (fig. S19A). The robotic sheet for plastic pollutants consists of a buoyancy skin with six muscles with 12-mm sides, a PEN base sheet with a thickness of 12 μm, and a wet-tolerant adhesive sheet that is composed of a soft double-sided adhesive (170 μm) and sticky elastomers (polydimethylsiloxane, Sylgard 186, Dow Corning). The total size and thickness are 15 cm by 15 cm and about 4 mm, respectively (fig. S20A). In addition, we constructed the robotic sheet for oil spills by incorporating capabilities of maneuverability, scalability, and oil absorbency into a single sheet platform (fig. S20D). To show the large-area feasibility, we designed a rapidly self-deployable origami base sheet that can also resist drag forces applied during swimming (Fig. 6, C and D). A base geometry was selected as a three-by-three Miura-ori pattern with total sides of 13.5 cm, and, subsequently, the ladybird beetle-inspired compliant origami (target radius of curvature, 88.45 mm) was designed into four sets of three collinear fold lines [see (44) for fabrication details]. The oil-skimming capability was added by the integration of superhydrophobic-superoleophilic membrane sheets (HP-156, 3M), which were cut into square units with sides of 18 mm. The total size and thickness are 13.5 cm by 13.5 cm and about 4 mm. The field experiment was conducted inside the chamber with dimensions of 90 cm by 90 cm by 60 cm. Reddish oil spills (NEW PSF-3, Hyundai) were artificially formed on the certain area of the water surface, bounded by a circular buoyant tube (Fig. 6E). The deployment of the origami sheet was passively triggered by dissolving the 3D printed, water-soluble string (diameter of 0.4 mm; polyvinyl alcohol, eSUN) that initially bound it.

### Buoyancy measurement

To measure the real-time buoyancy variation in muscles, a widely known hydrostatic weighing method was used (51). Although there were some limiting factors in this method, such as the meniscus formed around the suspension wire at the air-liquid interface and entrapped gas, we minimized them by decreasing the sample size and by conducting aging steps. An isolated system consisting of a muscle sample and a control weight (5 g) was set up and immersed into deionized (DI) water (~22°C) while connected only by thin conductive wires (fig. S6A). Upon activation, the muscle experienced variations in hydrostatic weight [ $\Delta w(t)$ ] as

$$\Delta w(t) = \rho_f \Delta V(t)$$

which allowed us to recalculate the time-dependent buoyancy [ $\Delta F_B(t)$ ] and density [ $\Delta \rho(t)$ ] values of the muscle. The operation window and characteristic profiles of buoyancy generation were measured by performing repeated heating (60 s) and cooling (30 s) steps at several different current levels from 0 to 0.35 A (Fig. 2G).

### Buoyancy characterization

The hydrostatic weighing method is effective in measuring the entire buoyancy variations but not in providing information of buoyancy distributions throughout spatial domains. To surmount this limitation, we established an alternative route for characterizing spatio-temporal buoyancy modulations. We found that buoyancy profiles

of more than 20 different activation conditions about input current, muscle geometry, and heating area could be reduced to a characteristic curve when normalized about the saturation buoyancy value (Fig. 2G). Without loss of generality, this governing curve could be expressed in the form of the first-order exponential decay curves, respectively, for the heating and cooling part:  $A_h + B_h \exp(-t/C_h)$  and  $A_c + B_c \exp(-t/C_c)$ , where the constants ( $A_h$ ,  $B_h$ , and  $C_h$ ) and ( $A_c$ ,  $B_c$ , and  $C_c$ ) can be determined by  $t_{0.2}$ ,  $t_{0.5}$ ,  $t_{0.8}$ , and  $t_{sat}$ , which are the time required for the buoyancy to reduce to 0.2, 0.5, 0.8, and 1 times its saturation value (fig. S7). On the basis of this indirect approach, we could successfully characterize transient responses of uniform buoyancy generation by the series of these generic buoyancy fitting curves (fig. S7, C to E). In addition, those of various nonuniform buoyancy modulations could be estimated by separate characterization in each activation site (fig. S13C), which provided us with qualitative information of buoyancy and torque distributions.

### Experimental setup for locomotion test

All swimming tests were performed in a 90 cm–by–90 cm–by–60 cm water chamber filled with DI water (fig. S23). Thin, insulated Cu wires (diameter, 22  $\mu\text{m}$ ) were connected to the swimming leaf and robotic sheets to apply the required power from the power supply (TDP-1003B, TOYOTECH). Because of the small diameter, the electrical resistance of the Cu wires ( $R_w \approx 35$  ohms) was needed to consider for control protocols. If necessary, then the density of the Cu wires was compensated by buoyant foam materials (density,  $\sim 0.77$  g  $\text{cm}^{-3}$ ). Three synchronized digital cameras were placed and captured the top, front, and side views with 60 frames per second (fps), the combination of which was used for the swimming analysis.

### Control protocol

The swimming locomotion of our swimming sheets were controlled by modulating buoyancy independently in three separate activation sites based on the underlying heating circuit design (fig. S5). Despite the reduced number of activation sites compared with the leaf design with nine mass spots in falling leaf experiments as shown in Fig. 1, this three-degrees-of-freedom control scheme enabled nearly continuous control of  $\delta$  instruction within a  $\delta$ -space, typically defined as a triangle in a swimming leaf and disk (Fig. 2E). Among a wide set of  $\delta$  instructions, we defined the seven representative control commands (fig. S16). Specifically, we used coupled pair combinations of two out of three activation sites due to the efficacy in delivering directional momentum by modulating  $\delta$  (Fig. 2E). The resultant buoyancy distributions could generate directional upward or downward flutter motions and vertical upward flutter motion (or transition between each mode). Depending on the desired swimming behaviors, seven different pairs of input voltages (or currents) could guide versatile gaits:  $U_k$  ( $k = 1, 2$ , and 3) for directional upward motions,  $D_k$  for directional downward motions, and Trans for transition states (fig. S16C). To produce such control commands, we designed a simple control circuit consisting of a microcontroller unit and pairs of high-voltage p-channel MOSFET (IRF9540, Devicemart, Korea) and n-channel MOSFET (IRL530N, Devicemart, Korea) (fig. S16B). Because of the nonnegligible electrical resistance of the Cu wires ( $R_w \approx 35$  ohms), we took it into account for control circuits. On the basis of the control circuit diagram, combinations of three different voltage levels ( $V_a$ ,  $V_b$ , and  $V_c$ ) could be selectively applied to three different activation sites ( $R_1 = R_2 = R_3 = R \approx 80$  ohms) of which currents ( $i_k$ ,  $k = 1, 2$ , and 3) are defined as

$$i_k = \frac{V_k}{R + R_w} - \frac{R_w(V_a + V_b + V_c)}{(R + R_w)(R + 4R_w)}$$

Each voltage value ( $V_a$ ,  $V_b$ , and  $V_c$ ) was selected such that the buoyancy generated by the corresponding current value satisfies (i)  $\Delta F_B > F_{th}$ , (ii)  $\Delta F_B \sim F_{th}$ , and (iii)  $\Delta F_B < F_{th}$ , respectively. For example, we determined the following set of voltage, ( $V_a$ ,  $V_b$ , and  $V_c$ ) = (19, 36.1, and 44.8 V), for swimming leaf demonstrations shown in Fig. 5 (D and E) and fig. S18.

### Data analysis

All 3D kinematics data were obtained by three synchronized digital cameras and analyzed by a free video analysis and modeling tool (Tracker 5.1.3). We first marked a black arrow on the base sheet of a swimming leaf and disk and filmed the swimming behaviors in 60 fps from three orthogonal views (top, front, and side). The center of mass position and angle of the marked arrow were analyzed in every 10 pixels ( $\sim 0.166$  s), and the relative coordinates and angles were used to calculate the full trajectory, velocity, acceleration, body angle, and angular velocity.

### SUPPLEMENTARY MATERIALS

[robotics.sciencemag.org/cgi/content/full/6/53/eabe0637/DC1](http://robotics.sciencemag.org/cgi/content/full/6/53/eabe0637/DC1)

Note S1. Conceptual design of a swimming leaf and disk.

Note S2. A quasi-steady 2D model for active flutter dynamics.

Note S3. Purpose and details of the experiments.

Note S4. Energy conversion efficiency of a swimming sheet.

Fig. S1. Falling styles of disks.

Fig. S2. Time-evolving horizontal movements of the falling leaf with a point mass located in different positions (P0 to P8).

Fig. S3. Definition of the principal flutter axis.

Fig. S4. Flutter dynamics modulation induced by inhomogeneous density distribution and corresponding reorientation of the principal flutter axis.

Fig. S5. Component design and structure of a swimming leaf and disk.

Fig. S6. Transient responses and characterization of a buoyancy skin.

Fig. S7. A strategy for estimating time-varying buoyancy responses.

Fig. S8. A swimming leaf based on a buoyancy skin.

Fig. S9. Geometric criterion for disk approximation.

Fig. S10. Kinematics of a swimming disk responding to quasi-static uniform buoyancy distribution (movie S2).

Fig. S11. Active flutter behaviors of a swimming disk under quasi-static uniform buoyancy distribution.

Fig. S12. Comparison and symmetry in dynamics of falling/swimming behavior.

Fig. S13. Directional active flutter behaviors of a swimming disk under quasi-static nonuniform buoyancy distribution (movie S3).

Fig. S14. Flutter axis reorientation in directional active flutter behaviors.

Fig. S15. Time-evolving flutter axis reorientation for steering control (movie S4).

Fig. S16. Control scheme for the swimming leaf.

Fig. S17. Straight, directional flutter gaits with depth maintenance.

Fig. S18. A long-term journey of a lifelike swimming leaf (movie S5).

Fig. S19. Ultraflexible swimming robotic sheet negotiating a small gap (movie S6).

Fig. S20. Swimming robotic sheets for marine environmental applications.

Fig. S21. A buoyancy skin for underwater cup manipulation (movie S9).

Fig. S22. A standard swimming disk under turbulence.

Fig. S23. Experimental setup for swimming locomotion and characterization.

Movie S1. A swimming leaf versus a falling leaf.

Movie S2. Active flutter of a swimming disk under uniform buoyancy distribution.

Movie S3. Directional active flutter of a swimming disk under nonuniform buoyancy distribution.

Movie S4. Versatile flutter swimming gaits through sequential reorientation of the principal flutter axis.

Movie S5. Long-term controlled maneuvering of a swimming leaf.

Movie S6. Demonstration of an ultraflexible swimming robotic sheet negotiating a small gap.

Movie S7. Demonstration of a swimming robotic adhesive sheet.

Movie S8. Demonstration of a swimming robotic oil-skimming sheet.

Movie S9. A buoyancy skin for underwater cup manipulation.

References (52–56)

## REFERENCES AND NOTES

1. P. Ern, F. Rizzo, D. Fabre, J. Magnaudet, Wake-induced oscillatory paths of bodies freely rising or falling in fluids. *Annu. Rev. Fluid Mech.* **44**, 97–121 (2012).
2. S. B. Field, M. Klaus, M. G. Moore, F. Nori, Chaotic dynamics of falling disks. *Nature* **388**, 252–254 (1997).
3. F. Augute, J. Magnaudet, D. Fabre, Falling styles of disks. *J. Fluid Mech.* **719**, 388–405 (2013).
4. L. Heisinger, P. Newton, E. Kanso, Coins falling in water. *J. Fluid Mech.* **742**, 243–253 (2014).
5. Y. Wang, C. Shu, C. J. Teo, L. M. Yang, Numerical study on the freely falling plate: Effects of density ratio and thickness-to-length ratio. *Phys. Fluids* **28**, 103603 (2016).
6. U. Pesavento, Z. J. Wang, Falling paper: Navier-Stokes solutions, model of fluid forces, and center of mass elevation. *Phys. Rev. Lett.* **93**, 144501 (2004).
7. L. Mahadevan, W. S. Ryu, A. D. T. Samuel, Tumbling cards. *Phys. Fluids* **11**, 1–3 (1999).
8. C. Magono, T. Nakamaru, Aerodynamic studies of falling snowflakes. *J. Meteorol. Soc. Jpn.* **43**, 139–147 (1965).
9. L. Vincent, W. S. Shambaugh, E. Kanso, Holes stabilize freely falling coins. *J. Fluid Mech.* **801**, 250–259 (2016).
10. U. Lacis, N. Brosse, F. Ingremoineau, A. Mazzino, F. Lundell, H. Kellay, S. Bagheri, Passive appendages generate drift through symmetry breaking. *Nat. Commun.* **5**, 5310 (2014).
11. T. Kim, J. Chang, D. Kim, Free-fall dynamics of a pair of rigidly linked disks. *Phys. Fluids* **30**, 034104 (2018).
12. W. Huang, H. Liu, F. Wang, J. Wu, H. P. Zhang, Experimental study of a freely falling plate with an inhomogeneous mass distribution. *Phys. Rev. E* **88**, 053008 (2013).
13. P. Paoletti, L. Mahadevan, Planar controlled gliding, tumbling and descent. *J. Fluid Mech.* **689**, 489–516 (2011).
14. G. Novati, L. Mahadevan, P. Koumoutsakos, Controlled gliding and perching through deep-reinforcement-learning. *Phys. Rev. Fluids* **4**, 093902 (2019).
15. R. Dudley, G. Byrnes, S. P. Yanoviak, B. Borrell, R. M. Brown, J. A. McGuire, Gliding and the functional origins of flight: Biomechanical novelty or necessity? *Annu. Rev. Ecol. Evol. Syst.* **38**, 179–201 (2007).
16. S. P. Yanoviak, R. Dudley, M. Kaspari, Directed aerial descent in canopy ants. *Nature* **433**, 624–626 (2005).
17. M. G. McCay, Aerodynamic stability and maneuverability of the gliding frog *Polypedates dennysi*. *J. Exp. Biol.* **204**, 2817–2826 (2001).
18. J. A. McGuire, R. Dudley, The cost of living large: Comparative gliding performance in flying lizards (Agamidae: *Draco*). *Am. Nat.* **166**, 93–106 (2005).
19. W.-S. Chu, K.-T. Lee, S.-H. Song, M.-W. Han, J.-Y. Lee, H.-S. Kim, M.-S. Kim, Y.-J. Park, K.-J. Cho, S.-H. Ahn, Review of biomimetic underwater robots using smart actuators. *Int. J. Precis. Eng. Manuf.* **13**, 1281–1292 (2012).
20. L. Hines, K. Petersen, G. Z. Lum, M. Sitti, Soft actuators for small-scale robotics. *Adv. Mater.* **29**, 1603483 (2017).
21. S.-J. Park, M. Gazzola, K. S. Park, S. Park, V. Di Santo, E. L. Blevins, J. U. Lind, P. H. Campbell, S. Dauth, A. K. Capulli, F. S. Pasqualini, S. Ahn, A. Cho, H. Yuan, B. M. Maoz, R. Vijaykumar, J.-W. Choi, K. Deisseroth, G. V. Lauder, L. Mahadevan, K. K. Parker, Phototactic guidance of a tissue-engineered soft-robotic ray. *Science* **353**, 158–162 (2016).
22. J. C. Nawroth, H. Lee, A. W. Feinberg, C. M. Ripplinger, M. L. McCain, A. Grosberg, J. O. Dabiri, K. K. Parker, A tissue-engineered jellyfish with biomimetic propulsion. *Nat. Biotech.* **30**, 792–797 (2012).
23. R. K. Katzschnmann, J. DelPreto, R. MacCurdy, D. Rus, Exploration of underwater life with an acoustically controlled soft robotic fish. *Sci. Robot.* **3**, eaar3449 (2018).
24. Z. Ren, W. Hu, X. Dong, M. Sitti, Multi-functional soft-bodied jellyfish-like swimming. *Nat. Commun.* **10**, 2703 (2019).
25. W. Hu, G. Z. Lum, M. Mastrangeli, M. Sitti, Small-scale soft-bodied robot with multimodal locomotion. *Nature* **554**, 81–85 (2018).
26. N. R. Sinatra, C. B. Teeple, D. M. Vogt, K. K. Parker, D. F. Gruber, R. J. Wood, Ultragentle manipulation of delicate structures using a soft robotic gripper. *Sci. Robot.* **4**, eaax5425 (2019).
27. Z. E. Teoh, B. T. Phillips, K. P. Becker, G. Whitredge, J. C. Weaver, C. Hoberman, D. F. Gruber, R. J. Wood, Rotary-actuated folding polyhedrons for midwater investigation of delicate marine organisms. *Sci. Robot.* **3**, eaat5276 (2018).
28. Z. Gong, X. Fang, X. Chen, J. Cheng, Z. Xie, J. Liu, B. Chen, H. Yang, S. Kong, Y. Hao, T. Wang, J. Yu, L. Wen, A soft manipulator for efficient delicate grasping in shallow water: Modeling, control, and real-world experiments. *Int. J. Robot. Res.* **40**, 449–469 (2021).
29. T. Xu, J. Zhang, M. Salehzadeh, O. Onaizah, E. Diller, Millimeter-scale flexible robots with programmable three-dimensional magnetization and motions. *Sci. Robot.* **4**, eaav4494 (2019).
30. J. Zhang, E. Diller, Untethered miniature soft robots: Modeling and design of a millimeter-scale swimming magnetic sheet. *Soft Robot.* **5**, 761–776 (2018).
31. H. Shahsavani, A. Aghakhani, H. Zeng, Y. Guo, Z. S. Davidson, A. Priimagi, M. Sitti, Bioinspired underwater locomotion of light-driven liquid crystal gels. *Proc. Natl. Acad. Sci. U.S.A.* **117**, 5125–5133 (2020).
32. A. Laskar, O. E. Shklyarev, A. C. Balazs, Designing self-propelled, chemically active sheets: Wrappers, flappers, and creepers. *Sci. Adv.* **4**, eaav1745 (2018).
33. G. I. Taylor, Analysis of the swimming of microscopic organisms. *Proc. R. Soc. London A* **209**, 447–461 (1951).
34. T. Y.-T. Wu, Hydromechanics of swimming propulsion. Part 1. Swimming of a two-dimensional flexible plate at variable forward speeds in an inviscid fluid. *J. Fluid Mech.* **46**, 337–355 (1971).
35. M. Argentina, J. Skotheim, L. Mahadevan, Settling and swimming of flexible fluid-lubricated foils. *Phys. Rev. Lett.* **99**, 224503 (2007).
36. N. T. Jafferis, H. A. Stone, J. C. Sturm, Traveling wave-induced aerodynamic propulsive forces using piezoelectrically deformed substrates. *Appl. Phys. Lett.* **99**, 114102 (2011).
37. A. Joshi, A. Kulkarni, Y. Taadesse, FludoJelly: Experimental study on jellyfish-like soft robot enabled by soft pneumatic composite (SPC). *Robotics* **8**, 56 (2019).
38. L. Wang, Y. Liu, Y. Cheng, X. Cui, H. Lian, Y. Liang, F. Chen, H. Wang, W. Guo, H. Li, M. Zhu, H. Ihara, A bioinspired swimming and walking hydrogel driven by light-controlled local density. *Adv. Sci.* **2**, 1500084 (2015).
39. A. Miriyev, K. Stack, H. Lipson, Soft material for soft actuators. *Nat. Commun.* **8**, 596 (2017).
40. E. J. Denton, J. G. Gilpin-Brown, The distribution of gas and liquid within the cuttlebone. *J. Mar. Biol. Assoc. UK* **41**, 365–381 (1961).
41. M. Gazzola, M. Argentina, L. Mahadevan, Scaling macroscopic aquatic locomotion. *Nat. Phys.* **10**, 758–761 (2014).
42. J. G. B. Derraik, The pollution of the marine environment by plastic debris: A review. *Mar. Pollut. Bull.* **44**, 842–852 (2002).
43. J. Beyer, H. C. Trannum, T. Bakke, P. V. Hodson, T. K. Collier, Environmental effects of the deepwater horizon oil spill: A review. *Mar. Pollut. Bull.* **110**, 28–51 (2016).
44. S.-M. Baek, S. Yim, S.-H. Chae, D.-Y. Lee, K.-J. Cho, Ladybird beetle-inspired compliant origami. *Sci. Robot.* **5**, eaaz6262 (2020).
45. J. Byun, Y. Lee, J. Yoon, B. Lee, E. Oh, S. Chung, T. Lee, K.-J. Cho, J. Kim, Y. Hong, Electronic skins for soft, compact, reversible assembly of wirelessly activated fully soft robots. *Sci. Robot.* **3**, eaas9020 (2018).
46. J. W. Booth, D. Shah, J. C. Case, E. L. White, M. C. Yuen, O. Cyr-Choiniere, R. Kramer-Bottiglio, OmniSkins: Robotic skins that turn inanimate objects into multifunctional robots. *Sci. Robot.* **3**, eaat1853 (2018).
47. S. Palagi, P. Fischer, Bioinspired microrobots. *Nat. Rev. Mater.* **3**, 113–124 (2018).
48. L. Shui, L. Zhu, Z. Yang, Y. Liu, X. Chen, Energy efficiency of mobile soft robots. *Soft Matter* **13**, 8223–8233 (2017).
49. S. M. Mirvakili, D. Sim, I. W. Hunter, R. Lagner, Actuation of untethered pneumatic artificial muscles and soft robots using magnetically induced liquid-to-gas phase transitions. *Sci. Robot.* **5**, eaaz4239 (2020).
50. M. Wang, D. Vecchio, C. Wang, A. Emre, X. Xiao, Z. Jiang, P. Bogdan, Y. Huang, N. A. Kotov, Biomimetic structural batteries for robotics. *Sci. Robot.* **5**, eaba1912 (2020).
51. N. A. Pratten, The precise measurement of the density of small samples. *J. Mater. Sci.* **16**, 1737–1747 (1981).
52. P. C. Fernandes, F. Rizzo, P. Ern, J. Magnaudet, Oscillatory motion and wake instability of freely rising axisymmetric bodies. *J. Fluid Mech.* **573**, 479–502 (2007).
53. H. Zhong, C. Lee, Z. Su, S. Chen, M. Zhou, J. Wu, Experimental investigation of freely falling thin disks. Part 1. The flow structures and Reynolds number effects on the zigzag motion. *J. Fluid Mech.* **716**, 228–250 (2013).
54. W. W. Willmarth, N. E. Hawk, R. L. Harvey, Steady and unsteady motions and wakes of freely falling disks. *Phys. Fluids* **7**, 197–208 (1964).
55. M. Rahmani, A. Wachs, Free falling and rising of spherical and angular particles. *Phys. Fluids* **26**, 083301 (2014).
56. G. Mougin, J. Magnaudet, The generalized Kirchhoff equations and their application to the interaction between a rigid body and an arbitrary time-dependent viscous flow. *Int. J. Multiphase Flow* **28**, 1837–1851 (2002).

**Funding:** This work was supported by a National Research Foundation of Korea (NRF) grant funded by the Korean Government (MSIP)(NRF-2016R1A5A1938472). J.B. appreciates the support from a NRF grant funded by the Korean Government (MSIT) (NRF-2020R1A6A3039466).

**Author contributions:** J.B., Y.H., and K.-J.C. conceived the idea. J.B. designed and fabricated the swimming leaves and robotic sheets, analyzed the performance, and developed the model. J.B., M.P., S.-M.B., and J.Y. conducted the experiments. J.B., M.P., and J.Y. established the control scheme. W.K. and B.L. developed tools for analysis. J.B. and K.-J.C. wrote the manuscript with input from all authors. **Competing interests:** J.B., M.P., and K.-J.C. are inventors on a patent application (KR. 10-2021-0046149) filed by Seoul National University. The other authors declare that they have no competing interests. **Data and materials availability:** All data are available in the main text or the Supplementary Materials.

Submitted 29 July 2020

Accepted 30 March 2021

Published 21 April 2021

10.1126/scirobotics.abe0637

**Citation:** J. Byun, M. Park, S.-M. Baek, J. Yoon, W. Kim, B. Lee, Y. Hong, K.-J. Cho, Underwater maneuvering of robotic sheets through buoyancy-mediated active flutter. *Sci. Robot.* **6**, eabe0637 (2021).

## Underwater maneuvering of robotic sheets through buoyancy-mediated active flutter

Junghwan Byun, Minjo Park, Sang-Min Baek, Jaeyoung Yoon, Woongbae Kim, Byeongmoon Lee, Yongtaek Hong and Kyu-Jin Cho

*Sci. Robotics* **6**, eabe0637.  
DOI: 10.1126/scirobotics.abe0637

### ARTICLE TOOLS

<http://robotics.sciencemag.org/content/6/53/eabe0637>

### SUPPLEMENTARY MATERIALS

<http://robotics.sciencemag.org/content/suppl/2021/04/19/6.53.eabe0637.DC1>

### RELATED CONTENT

<http://robotics.sciencemag.org/content/robotics/5/41/eaaz6262.full>  
<http://robotics.sciencemag.org/content/robotics/3/18/eaas9020.full>  
<http://robotics.sciencemag.org/content/robotics/4/33/eaax5425.full>

### REFERENCES

This article cites 56 articles, 3 of which you can access for free  
<http://robotics.sciencemag.org/content/6/53/eabe0637#BIBL>

### PERMISSIONS

<http://www.sciencemag.org/help/reprints-and-permissions>

Use of this article is subject to the [Terms of Service](#)

---

*Science Robotics* (ISSN 2470-9476) is published by the American Association for the Advancement of Science, 1200 New York Avenue NW, Washington, DC 20005. The title *Science Robotics* is a registered trademark of AAAS.

Copyright © 2021 The Authors, some rights reserved; exclusive licensee American Association for the Advancement of Science. No claim to original U.S. Government Works